Runoff-generated debris flows: Observation of initiation conditions and erosion–deposition dynamics along the channel at Cancia (eastern Italian Alps)

Alessandro Simoni,[1]* iD **Martino Bernard,**[2] iD **Matteo Berti,**[1] iD **Mauro Boreggio,**[2] **Stefano Lanzoni,**[3] iD
Laura Maria Stancanelli[4,5] iD **and Carlo Gregoretti**[2] iD

[1] Department BiGeA, University of Bologna, via Zamboni 67, Bologna 40126, Italy
[2] Land Environment Agriculture and Forestry Department, University of Padova, viale dell'Università 16, Legnaro 35020, Italy
[3] Civil, Environmental and Architectural Engineering Department, University of Padova, via Loredan 20, Padova 35131, Italy
[4] Environmental and Civil Engineering Department, University of Catania, Piazza Università 2, Catania 95131, Italy
[5] Swiss Federal Institute for Forest, Snow and Landscape Research, WSL, Switzerland

*Correspondence to: Alessandro Simoni, Department BiGeA, University of Bologna, via Zamboni 67, 40126 Bologna, Italy. E-mail: alessandro.simoni@unibo.it

ESPL
Earth Surface Processes and Landforms

ABSTRACT: In the Dolomitic region, abundant coarse hillslope sediment is commonly found at the toe of rocky cliffs. Ephemeral channels originate where lower permeability bedrock surfaces concentrate surface runoff. Debris flows initiate along such channels following intense rainfall and determine the progressive erosion and deepening of the channels. Sediment recharge mechanisms include rock fall, dry ravel processes and channel-bank failures. Here we document debris flow activity that took place in an active debris flow basin during the year 2015. The Cancia basin is located on the southwestern slope of Mount Antelao (3264 m a.s.l.) in the dolomitic region of the eastern Italian Alps. The 2.5 km^2 basin is incised in dolomitic limestone rocks. The data consist of repeated topographic surveys, distributed rainfall measurements, time-lapse (2 s) videos of two events and pore pressure measurements in the channel bed. During July and August 2015, two debris flow events occurred, following similarly intense rainstorms. We compared rainfall data to existing rainfall triggering thresholds and simulated the hydrological response of the headwater catchment with a distributed model in order to estimate the total and peak water discharge. Our data clearly illustrate how debris entrainment along the channel is the main contributor to the overall mobilized volume and that erosion is dominant when the channel slope exceeds 16°. Further downstream, sediment accumulation and depletion occurred alternately for the two successive events, indicating that sediment availability along the channel also influences the flow behaviour along the prevailing-transport reach. The comparison between monitoring data, topographical analysis and hydrological simulation allows the estimation of the average solid concentration of the two events and suggests that debris availability has a significant influence on the debris flow volume. © 2020 John Wiley & Sons, Ltd.

KEYWORDS: debris flow; runoff initiation; rainfall thresholds; erosion

Introduction

In alpine areas, abundant coarse hillslope sediment is commonly found at the toe of rocky cliffs. Channels originate where the bedrock surfaces deliver surface runoff, at the outlet of chutes incised into the cliffs. Debris flows initiate along such channels following intense rainfall and determine the progressive erosion and deepening of the channels. This type of runoff-generated debris flow is common in alpine areas (Imaizumi *et al.*, 2006; Coe *et al.*, 2008; Hurlimann *et al.*, 2013; Theule *et al.*, 2015) but was observed also in recently burned steeplands (Cannon *et al.*, 2001; Kean *et al.*, 2011), steep volcanic terrain (Lavigne and Thouret, 2003; Okano *et al.*, 2012; Capra *et al.*, 2018) and other environments (Ma *et al.*, 2018).

The mechanism of transformation of loose debris into flowing debris generated by water runoff is not fully understood. However, there is general consensus on the fact that the material susceptible to mobilization is represented by the loose sediment accumulated on the bed of the debris flow channel. This channel-bed material may undergo localized mass failure with consequent sediment entrainment by hydrodynamic forces (Takahashi, 1991; Kean *et al.*, 2013) or, more simply, may be subject to progressive erosion by hydrodynamic forces from the top down. Evidence of this latter mechanism was found in flume experiments (Tognacca *et al.*, 2000; Hu *et al.*, 2016) and in the field (McCoy *et al.*, 2012) and models were proposed to describe the incipient motion of particles on steep slopes (Lamb *et al.*, 2008; Recking, 2009). Regardless of the precise mobilization mechanism, debris flow

initiation requires the presence of sediment deposits along the channel bed. Their abundance and distribution, together with the rainfall characteristics, influence the frequency and magnitude of debris flow events. Bovis and Jakob (1999) first recognized the possible existence of two limit classes of debris flow basins, weathering-limited and transport-limited, based on debris availability in relation to climate forcing. They stressed the importance of sediment recharge rates in weathering-limited systems where debris production is a controlling factor for debris flow frequency. At the other end of the spectrum, it is unclear whether basins where the availability of sediments is truly unlimited do exist, such that the occurrence of debris flow becomes transport-limited. In any case, the process of channel infilling assumes notable relevance for debris flow initiation in the vast majority of basins. Sediment recharge mechanisms include rock fall and dry ravel processes following debris flow (Coe et al., 2008; Loye et al., 2016; Rengers et al., 2020), channel-bank failures (Berti and Simoni, 2005), bed load by water flow and/or very small debris flows (Kean et al., 2013) and landsliding (Berger et al., 2011).

Unfortunately, a limited amount of field observations exist that can be used to evaluate how channel-bed material availability may influence debris flow initiation and magnitude for a given set of topographic and hydrologic conditions. Such observations are scarce because events are usually infrequent and the terrain is typically difficult to access. Pioneering studies include Jakob et al. (2005) who constrained debris recharge rates over time for weathering-limited bedrock-incised channels and Imaizumi et al. (2006) who documented with geomorphological observations sediment infilling of steep channels and subsequent periodic evacuation. Mao et al. (2009) showed how sediment recharge rates can profoundly influence the morphology and sediment-transport behaviour of otherwise similar catchments while Imaizumi et al. (2017) documented the influence of sediment availability and rainfall pattern on the type of flow that can be generated in a small debris flow catchment. Direct measurements of the entrainment rates of full-scale debris flows have been obtained at only a few field sites (Berger et al., 2011; McCoy et al., 2012). Additional information on the total volume of eroded material is available from periodic or event-based topographic differencing (Schürch et al., 2011; Blasone et al., 2014; Theule et al., 2015; Loye et al., 2016; Vázquez et al., 2016; Ma et al., 2018); however, the full depth of erosion can sometimes be obscured by deposition during the tail of the flow (Staley et al., 2011). Efforts to include sediment availability in the prediction of debris flow magnitude and frequency have started in the last few years (Jakob and Friele, 2010; Loye et al., 2016; Jakob et al., 2017) but challenges and limitations are still relevant for practical applications (Rickenmann, 2016), therefore direct observations are still in great need.

In this paper, we document debris flow activity that took place in an active basin of the eastern Italian Alps in the year 2015. During July and August, only 12 days apart, two debris flow events occurred, following rainstorms of similar intensity. Data consist of repeated topographic surveys of the debris flow channel, distributed rainfall measurements and time-lapse (2 s) videos of two events at the initiation area, and pore pressure measurements in the channel bed. The objectives of this are to identify the factors governing erosion and deposition along the channel and to assess the impact of sediment availability on the magnitude of the two documented events.

We analysed triggering rainfalls and compared them to previous known events and non-triggering rainfalls to evaluate the performance of existing duration–intensity thresholds. We used hydrological modelling to estimate the timing and magnitude of liquid discharge at a monitoring station placed in the initiation area of the debris flows. The collected data document the surging nature of the flow and allowed us to compare simulated and observed hydrological timing. Images of the events were used to estimate the height and speed of the debris flow front in conjunction with pore pressures measured at the base of the flow.

Pre- and post-event topographies were compared to investigate erosion–deposition dynamics in relation to the slope of the debris flow channel and its local morphology. Given that events were triggered by similar rainfalls, we analysed their differences in terms of overall mobilized volume and patterns of erosion and deposition to gain insight into the possible effect of sediment availability on debris flow volume. The combination of field observations with predictions from a hydrological model allowed us to estimate and then compare the overall sediment concentration of the two events.

Materials and Methods

The study site

The Cancia basin is located on the southwestern slope of Mount Antelao (3264 m a.s.l.) in the dolomitic region of the eastern Italian Alps. The 2.5 km^2 basin is incised in dolomitic limestone rocks. Steep bedrock cliffs dominate the headwater and produce abundant unconsolidated scree deposits. Scree slopes are near the angle of repose, sparsely vegetated by shrubs below 2000 m and covered by alpine forests below 1600 m a.s.l. The Cancia basin is in fact composed of two sub-basins (Figure 1a). Though similar in size, they differ in the relative abundance of loose unconsolidated debris vs. outcropping or subcropping bedrock. In the west sub-basin (0.73 km^2) vegetated scree deposits extend over 27% of the area and bare loose debris represent 22% (Figure 1b). Conversely, in the east sub-basin, bare scree accounts for only 5% and vegetated scree patches are scattered on top of largely dominant dolomite outcrops/subcrops (62% of the area). Debris flows represent the main sediment transport mechanism for the west sub-basin, whereas in the east sub-basin (0.99 km^2) regular torrential activity is largely dominant and sediment is mostly transported by bedload transport. The confluence is located at an elevation of 1320 m along the large debris flow fan. The small village of Cancia (Borca di Cadore municipality) is located at the toe of the fan and is protected by a series of check dams built in the lower part of the channel and two in-series sediment retention basins (Figure 1a) positioned at elevations of 1340 and 1000 m a.s.l., respectively.

Debris flows are triggered by the surface water runoff that steep rocky slopes concentrate into the headwater. They initiate along the channels incised in the scree deposits and then propagate downstream, entraining the channel-bed material and contributing to the deepening of the drainage network (Figures 2b and c). Scree deposits are generally unconsolidated, nevertheless, probably due to the stress and age increasing with depth, they are consistently more dense and coherent than the sediment filling the channel bed, characterized by an extremely loose open structure.

Channel-bed material accumulates along the channel due to rockfall from dolomite cliffs and dry ravel from steep channel banks, promoted by drying and wetting cycles. Results of grain-size measurements indicate that the coarse fraction is largely dominant, while sand and fines add up to 15% on average (Figure 3). Similar results were found by
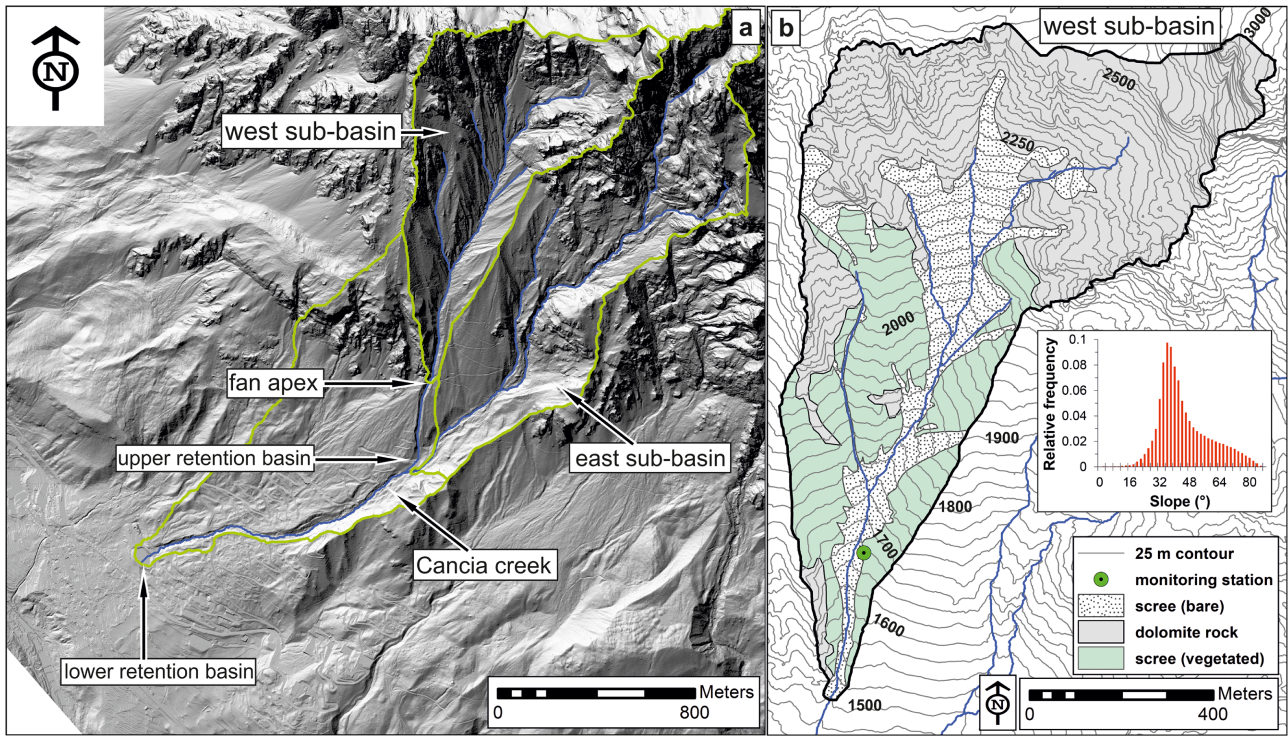
Figure 1. Cancia study basin. (a) Shaded relief map with identification of the two headwater sub-basins. (b) Schematic geological map of the west sub-basin showing instrumentation and main morphological features of the debris flow channel. The small inset shows the slope frequency distribution. [Colour figure can be viewed at wileyonlinelibrary.com]
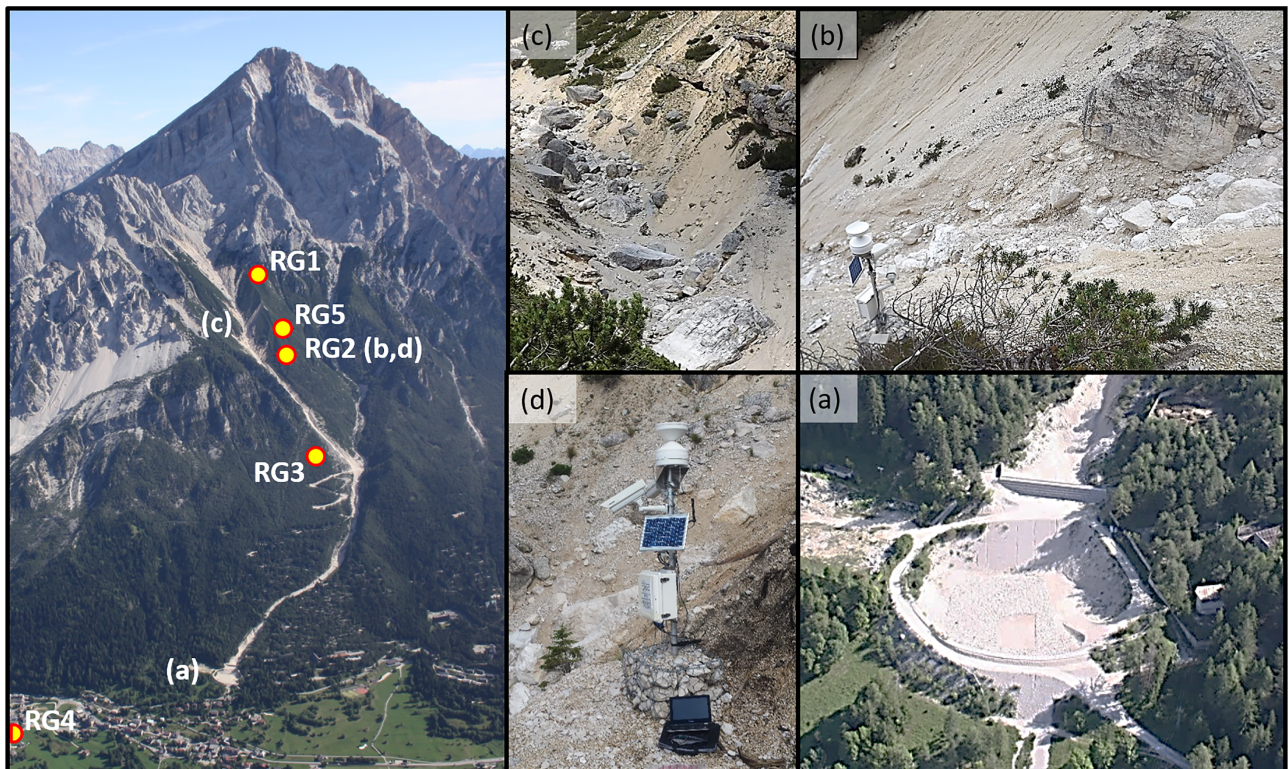

Figure 2. Photographs showing the Cancia study basin and the location and numbering of raingauges (RG) used for this study. Inset photographs show: (a) the lower sediment retention basin closes off the debris flow channel on the fan; (b) the location of the monitoring station overlooking the debris flow initiation area; (c) the debris flow channel in the upper part of the initiation area (looking upstream) where mega-boulders become more abundant at the expense of loose debris; (d) the monitoring station including two cameras, two pressure sensors buried in the channel bed and a raingauge. [Colour figure can be viewed at wileyonlinelibrary.com]

Gregoretti *et al.* (2019) for deposits of previous flow events. Debris flow activity evacuates accumulated sediment, erodes the channel and underscours its bank, causing frequent localized bank failures that foster the cyclic process of channel filling. Triggering rainfalls consist of short and intense rainfalls typically produced during the summer season by convective rainstorms (Berti and Simoni, 2005; Underwood *et al.*, 2016).
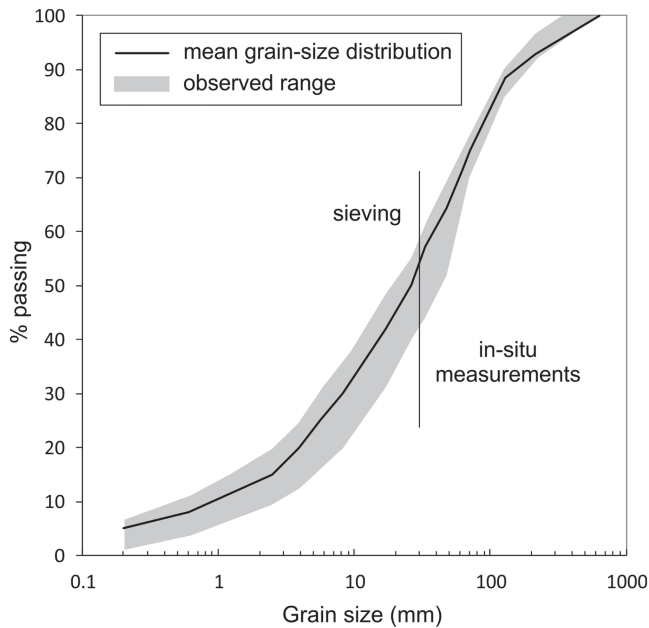
Figure 3. Grain-size distribution of channel-bed material. Results derive from combined *in-situ* measurements (frequency by weight method) and lab sieving (5 kg samples) performed during spring 2015 in four locations of the channel bed in the initiation area (elev.: 1700–1600 m a.s.l.).

Monitoring activities

In June 2014, we installed a low-cost monitoring station along the debris flow channel at an elevation of 1665 m (Figures 2b and d). Here the channel is steep (about 30°) and debris flow initiation occurs due to erosion of the channel bed material. The aim of the monitoring was to gain knowledge of the channel runoff and debris flow initiation by measuring pore-water pressures in the channel-bed material and recording time-lapse videos of the channel during and after intense rainfalls. Measured parameters also include 5-min rainfall intensity and wind speed and direction.

We acquired high-frequency data (5 s) measured by two pressure sensors buried in the channel-bed material, whenever a rainfall intensity threshold ($0.3 \, mm \, min^{-1}$) was exceeded. At the same time, the two time-lapse cameras were powered by a datalogger and started recording high-resolution (1280×720) images at a frequency of 0.5 Hz to document channel dynamics following intense rainfalls. During regular functioning, data (rainfall, pressures) were acquired every 5 min by the datalogger and cameras were off. Pressures were measured by piezoresistive differential pressure transducers with a nominal accuracy of 0.1 mm of water pressure (measuring range: 0–50 kPa) buried 20 cm below the channel bed. Cameras recorded HD images, storing them on a 32 GB SD card.

In the Cancia basin, a warning and alarm system is also operating. It is based on multiple distance and wire sensors deployed along the debris flow channel in four stations. Data are always recorded every minute and are therefore of limited use for debris flow documentation. The warning system has no connection to our monitoring system. However, we took advantage of the raingauges connected to the warning system to increase the spatial resolution of rainfall measurement (Figure 2).

Topographic and UAV surveys

In order to document the morphological changes caused along the main flow channel by the two debris flow events that occurred during summer 2015, we use topographical information acquired at different dates, mainly for civil protection purposes. They consist of one airborne laser scanning survey performed in 2011 (ground points spacing equal to about 0.85 m) and two series of unmanned aerial vehicle (UAV) aerial photographs taken shortly after the two events (ground points spacing equal to about 0.10 m). We used these surveys to obtain 1 m digital elevation models (DEMs).

We also repeatedly surveyed the channel to document its changes by means of photos and local topographic measurements performed using mainly the GPS-RTK technique and, on one occasion, terrestrial laser scanning (TLS). GPS-RTK surveys consisted of measuring cross-sections along the channel (precision < 0.1 m) and were carried out in October 2013 and October 2015. The TLS survey dates back to December 2014 and covers the channel between 1300 and 1650 m a.s.l. approximately (mean absolute registration error < 0.03 m, ground point spacing ~ 0.15 m).

Topographic data of ground-based surveys performed between October 2013 and December 2014 were used to update the 2011 LiDAR-derived DEM, thus obtaining a reliable depiction of the 2015 pre-event channel morphology (Table 1). The updates mainly concerned the upper part of the debris flow channel, where two small-to-medium size events occurring in the summer of 2013 caused localized topographic changes (see Table 3 later). It is noteworthy during field surveys conducted before July 2015 that we detected only minor changes in channel morphology with respect to autumn–winter 2013–2014, mainly related to dry ravels from channel banks that slowly recharge the channel bed with sediments. The resulting DEM can be considered representative of the channel morphology before the event occurred on 23 July.

We derived two post-event DEMs from aerial photographs taken shortly after the debris flow events of July and August 2015. They cover the unvegetated channel area from the lower sediment retention basins to our monitoring station. Only the areas of the upper (1340 m a.s.l.) and lower retention basin (1000 m a.s.l.) excavation works, aimed to re-establish the functionality of protection structures, caused minor topographical

Table 1. DEMs used for pre-/post-event topography comparisons, cell size is 1 m. Median vertical errors and standard deviation of vertical errors result from the accuracy analysis of DEMs using independent GPS-RTK measures as ground control points

DEM	Survey technique	Survey date	Median vertical error (m)	Standard deviation of vertical errors (m)
23/07/2015 pre-event	LiDAR 2011 + GPS and TLS surveys[a]	2011 to 2014 December	−0.044	0.255
23/07/2015 post-event	aerial photo restitution + GPS[b]	31/07/2015	−0.082	0.475
04/08/2015 pre-event	aerial photo restitution	31/07/2015	−0.082	0.475
04/08/2015 post-event	aerial photo restitution	06/08/2015	0.054	0.636

[a]GPS and TLS surveys executed along the channel have been used to update the 2011 LiDAR-derived topography.
[b]On 24 July GPS-RTK surveys were executed in the upper and lower sediment retention basins; the results were used to locally modify the DEM obtained by aerial photo or the 31 July UAV flight.

variations during the few days between each event and the corresponding UAV flights (8 and 2 days, respectively). After the first event, GPS-RTK surveys allowed us to eliminate inaccuracies due to post-event excavations (Table 1). In the case of the second event, excavations executed inside the upper retention basin between 31/07 and 04/08 account for an estimated 1000 m³ (based on the number of vehicles used for transport) that are erroneously included in the 04/08 pre-event DEM (Table 1). Similarly, the 04/08 post-event DEM does not account for 500 m³ of material excavated the following day before aerial photos were taken. Such inaccuracies are limited to the upper sediment retention basins and are deemed to not impair our ability to document the relevant morphological changes produced by the debris flow event along the channel.

In this paper, pre- and post-event channel topographies are used to map erosion–deposition patterns. We calculated elevation-change models from subsequent surveys. Independent GPS-RTK measurements acquired in correspondence with stable morphological features (e.g. check dams and retentions basin) were used as ground control points in order to assess the vertical accuracy of each generated terrain model. Furthermore, stable areas immediately outside the gully that did not reasonably experience any elevation change within the reference time period were used to evaluate the relative accuracy of pre- and post-event DEMs. In particular, elevation accuracies were evaluated through the approach developed by Höhle and Höhle (2009) and Höhle and Potuckova (2011). The systematic error of each DEM has been corrected by a 2.5D calibration along the vertical axis before evaluating the DEM of difference (DoD). As highlighted by various authors (e.g. Lane *et al.*, 2003; Wheaton *et al.*, 2010), when performing operations of difference between multi-temporal DEMs, it is essential to take into account the intrinsic error of each individual DEM. This allows us to distinguish the real morphological changes by the noise of the DEMs, reaching a theoretically more accurate volumetric balance. In order to filter uncertainties inherent to pre- and post-event DEMs, we applied a threshold (minimum level of detection) calculated by propagating as quadratic sum the standard deviations of vertical errors of each DEM (Brasington *et al.*, 2003). The resulting minimum level of detection was 0.539 m for the 23 July event and 0.794 m for the 4 August event. Below these thresholds, elevation changes were neglected in our DoD models.

The hydrological model

We used a modelling approach to simulate the surface runoff generated by the rainfall episodes that triggered the observed debris flows. Model results are checked in terms of peak timing and duration of runoff against the data acquired by the monitoring station located in the initiation area (Figure 1b).

Specifically, we used the distributed hydrological model developed by Gregoretti *et al.* (2016) for small rocky headwater catchments. Here we briefly summarize the main features of this model, referring the reader to Gregoretti *et al.* (2016) for further details. The model consists of a DEM-based method whereby the excess rainfall is computed for each pixel and routed to the outlet. Along the steepest path of slope, a constant slope velocity U is assumed, depending on the terrain typology; along the channel network, a matched diffusivity kinematic model is employed (i.e. the Muskingum–Cunge scheme implemented by Orlandini and Rosso, 1996). Excess rainfall is computed through either a simplified Horton's law when rainfall intensity exceeds infiltration rate (f_C) or by using the SCS-CN method (SCS, 1972; NRCS, 2008). The rainfall input to the model is calculated for each pixel from the data measured by

raingauges 1 and 2 (Figure 2). The corresponding areas of influence are determined by means of the Thiessen polygons.

The relevant parameters of the model are the curve number CN, the critical infiltration rate f_C – leading to runoff inception, the along-slope velocity U and the friction coefficient for channel routing K_S. Their typical values are reported in Table 2 and were set equal to those estimated by Gregoretti *et al.* (2016) in a dolomitic headwater basin (Dimai) with morphology similar to Cancia. In the Dimai basin, these values have been found to reproduce with good accuracy peak discharge, volume and overall shape (i.e. the nearly vertical initial rise and the slower decreasing limb) of five runoff hydrographs directly measured in the field. According to the SCS-CN method, the critical infiltration rate that provides most of the runoff for a rocky terrain depends on the rainfall depth of the previous 5 days. However, the analysis carried out by Bernard (2018) on the basis of further runoff measurements (12) collected at Dimai and runoff estimates (220) concerning the dolomitic basins of Dimai, Punta Nera and Cancia itself suggests a dependence of f_C on moisture conditions antecedent to rainfall (AMC; Chow *et al.*, 1988) of the previous 2 days. Therefore, both the debris flow events investigated here were characterized by AMCI conditions. Note also that the average f_C values reported in Table 2 typical of scree slopes and mountain pine slopes are likely to be seldom exceeded by rainfall rate and, consequently, their influence on the model output is negligible.

We used the predictions of the hydrological model to compute the response of the headwater catchment in the debris flow initiation area where the monitoring station is located. Given that the entrainment of sediment is still limited in the initiation area (Rengers *et al.*, 2016), we assume that the hydrological simulations hold in terms of timing (time to peak, duration) and water discharge.

Historical Data and Rainfall Threshold for Debris Flow Initiation

The Cancia catchment has a long history of debris flow activity and, given the presence of a village on its fan, some historical information is available. The largest recorded debris flow event dates back to 27 July 1868. It deposited more than 100 000 m³ of debris, caused severe damage to the village and reached the Boite River, temporarily damming its course (Bacchini and Zannoni, 2003). After World War II, the historical record becomes progressively more complete and destructive events are described in 1966, 1987, 1994 and 1996. We collected available information about rainfall triggering major events and associated volumes of mobilized debris. These data are summarized in Table 3, together with those directly collected by the authors for the most recent events (1999–2019).

Runoff-generated debris flows are commonly triggered by very intense rainfall, with duration often less than 1 h (Berti and Simoni, 2005; Coe *et al.*, 2008; Underwood *et al.*, 2016; Bel *et al.*, 2017). The definition of rainfall events is thus crucial to isolate episodes of high-intensity rainfall. We define a

Table 2. Values of the parameters used in the hydrological model

Parameter	Rocky surface	Mountain pine slopes	Scree slopes
CN	90.4	61	65–70
U (ms^{-1})	0.7	0.05	0.1
K_S (m$^{1/3}$ s^{-1})	9	9	9
f_C (cmh^{-1})	3.5[*]	5.5	10.8

[*] From Bernard (2018).

Table 3. Debris flow events occurring in the Cancia basin and parameters of the triggering rainfall. For each event, rainfall data are those provided by the available raingauge closest to the headwater basin (see Figure 2 for location); rainfall duration/intensity are determined in accordance with the definition given in the text (BIT = 0.2 mm per 5 min)

Date	Volume (m³)	Raingauge	Rainfall duration (h)	Rainfall intensity (mm h⁻¹)	Maximum rainfall intensity[g] (mm h⁻¹)
27/07/1868[a,b]	10000	N/A	–	–	–
27/05/1957[a,b,c]	25000	N/A	–	–	–
05/11/1966[a,b,c]	25000	N/A	–	–	–
19/07/1987[a,b,c]	15000	N/A	–	–	–
12/07/1989	N/A	4	0.50	43.20	0
02/07/1994[a,b]	30000	4	1.42	17.36	64.8
07/08/1996[a,b,c]	40–50000	4	0.58	44.91	141.6
16/08/1999[d]	5000–7000	5	3.42	9.01	24
18/07/2009[e]	50000	3	1.17	20.57	74.4
26/07/2013[f]	9000	4	1.17	18.51	38.4
19/08/2013[f]	5000	5	1.50	21.47	93.6
23/07/2015	28850	1	2.17	20.49	98.4
04/08/2015	22770	1	1.83	24.22	118.8
25/06/2017	<4000	1	4.58	9.91	79.2
05/07/2018	<4000	1	1.42	25.76	85.2
01/08/2018	4000	1	3.83	11.45	88.8
29/10/2018	12000	3	6.67	20.97	91.2

Sources: [a]Mantovani *et al.* (2002); [b]Bacchini and Zannoni (2003); [c]Panizza *et al.* (1998); [d]Tropeano *et al.* (1999); [e]Gregoretti *et al.* (2019); [f]Degetto *et al.* (2015).
[g]Measured over 5 min.

high-intensity rainfall episode, or 'burst' (Coe *et al.*, 2008), as a segment of rainfall that begins when the intensity equals or exceeds a given threshold (burst intensity threshold, BIT in the following) and ends when the intensity drops below such a value for longer than 10 min. By adopting a BIT equal to 0.2 mm per 5 min (our rainfall measurement interval), we identified more than 7000 rainfall episodes for raingauges 1, 2 and 3 (Figure 2) in the 2014–2019 period. The same criteria were used to measure rainfall bursts that triggered the events listed in Table 3. In the following, we compare our data with existing rainfall thresholds for debris-flow initiation to check their validity at Cancia, also in relation to spatial rainfall variability.

Rainfall intensity (*I*)–duration (*D*) thresholds are typically represented by a power law equation, $I = \alpha D^{\beta}$, where α and β are empirically derived constants. According to Staley *et al.* (2013), thresholds are based on the following two assumptions: rapid and nonlinear increases of debris flow probability with increasing rainfall intensity at and above the threshold; low to null probability below the threshold. The power law describes rainfall intensities decreasing with duration according to the constant β. The literature reports numerous rainfall *ID* thresholds for debris flow occurrence that are differentiated based on: (i) the type of hydrological response of the headwater catchment (influence of soil type and morphology); (ii) the type of debris flow (runoff-generated or landslide-induced); (iii) the methodology used to derive the threshold. Regarding this latter issue, upper limit approaches define a threshold based on the maximum rainfall intensity that did not cause debris flow, while lower limit approaches are based on the lowest intensities that caused a debris flow (Staley *et al.*, 2013).

We compared our data with selected lower limit rainfall *ID* thresholds derived for debris flow occurrence in the dolomitic area (Figure 4). Bacchini and Zannoni (2003), Berti and Simoni (2005) and Gregoretti and Dalla Fontana (2007) derived their thresholds by visual inspection of points associated with triggering rainfalls in the intensity–duration chart. We also compared to the upper limit threshold proposed by Staley *et al.* (2013) for Southern California that was derived by an objective function. The comparison indicates that the two very similar thresholds proposed by Berti and Simoni (2005) and Gregoretti and Dalla Fontana (2007) are capable of separating

high-intensity rainfall episodes that triggered debris flows from the vast majority of other intense rainfall episodes that did not cause debris flows. Conversely, the thresholds proposed by Bacchini and Zannoni (2003) and Staley *et al.* (2013) appear too conservative and would lead to the identification of tens of false triggering rainfall events in the considered 6-year period alone.

All the rainfall that triggered major debris flow events (>10000 m³) is correctly identified by the highest thresholds and the two false negative cases visible in Figure 4 correspond to small events that occurred in August 1999 and July 2013 (Table 3). Conversely, the number of false positive rainfall
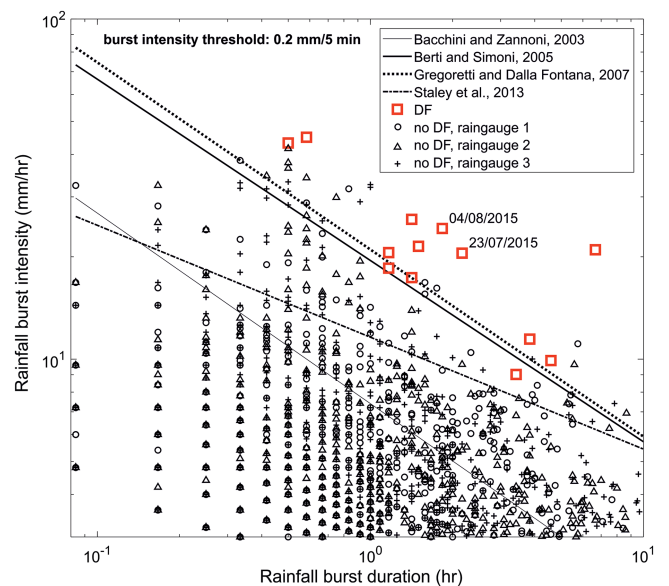

Figure 4. Triggering and non-triggering rainfalls measured at Cancia and compared to existing rainfall thresholds. Rainfall bursts begin when the intensity equals or exceeds 0.2 mm per 5 min (burst intensity threshold) and ends when the intensity drops below such value for longer than 10 min. Triggering rainfalls are listed in Table 3. Non-triggering rainfalls were measured by raingauges 1, 2 and 3 (see Figure 2 for location) during the 6-year period 2014–2019. [Colour figure can be viewed at wileyonlinelibrary.com]

events recorded by raingauges 1, 2 and 3 (Figure 2) is relatively low when compared to the total number of recorded rainfall events (Table 4). Such a result, obtained with a simple two-parameter description of rainfall events, suggests that antecedent rainfall might play a minor role in a basin dominated by carbonate rock outcrops and coarse granular debris.

In order to test the influence of rainfall burst definition on the analysis, we calculated rainfall *ID* parameters for increasing values of the intensities required to commence and end the burst (BIT) and verified the result against the rainfall *ID* threshold proposed by Gregoretti and Dalla Fontana (2007). Numerical results are reported in Table 4. When increasing the burst intensity threshold by a factor of two (0.2 to 0.4 to 0.8 mm per 5 min), we find a marginal improvement in the true positive rate (11/13 to 12/13) that is counterbalanced by higher false positive rates caused both by the increase of false positives and the decrease of identified rainfall episodes. An objective measure of the performance associated with the *ID* threshold classification may be obtained by means of a receiving operating characteristic (ROC) method (Swets, 1988). We have thus computed ROC curves by varying the empirical parameter α while keeping the exponent constant ($\beta = -0.55$) in the *ID* power law threshold. Table 4 reports the area under the curve (AUC) values that provide an aggregate measure of performance across all possible thresholds. They are all very high (>0.93), indicating that the rainfall *ID* model performs very well in separating triggering and non-triggering rainfalls. Marginally higher AUC values, associated with the lowest rates of false positives, are obtained for the raingauge located in the headwater catchment (i.e. nearby the initiation area). This result suggests that, owing to the relatively high spatial variability of intense rainfall events, it is important to place the raingauge as close as possible to the debris flow initiation zone. We also used the critical success index [CSI = tp/(tp + fn + fp), also known as the 'threat score'] as an aggregate measure of performance to find ideal α values. The results (Table 4) indicate that α should range between 20 and 23.6, an interval very close to the value of 21 derived by visual inspection by Gregoretti and Dalla Fontana (2007).

Despite the overall satisfactory performance of the rainfall *ID* threshold at Cancia, our analysis demonstrates that there is no perfect separation between triggering and non-triggering rainfall in the *ID* space. The main factors likely contributing to this observation are reviewed in the discussion section.

Monitored Debris Flow Events: 23 July and 4 August 2015

During the summer of 2015, two debris flows occurred at Cancia with an interval of just 12 days. The two events were triggered by similar short and intense rainfall events. When

calculated with the criteria described above, durations and intensities were 130 min and 20.49 mm h^{-1} for the first event and 110 min and 24.22 mm h^{-1} for the second event. Figure 5 shows the cumulative rainfalls measured by the raingauges operating in the Cancia basin (Figure 2). The differences are striking, with notably higher intensities measured by the instrument positioned in the headwater portion of the basin at higher elevation. Also, the timing of measurements shows that the rainstorm cells locally travelled from northeast to southwest. On 23 July, raingauges 2 and 3 started their mea-
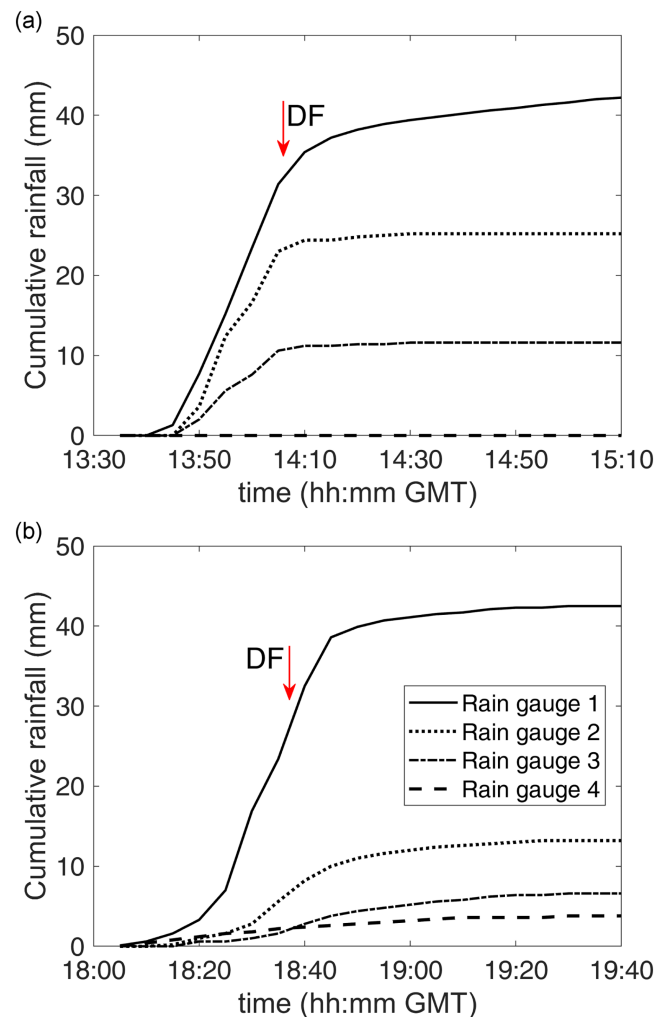

Figure 5. Cumulative rainfall depths recorded by raingauges 1, 2, 3 and 4 for the two events of 23 July (a) and 4 August (b). The timing of debris/hyperconcentrated flow transits at the monitoring station is pointed out by the arrows. Refer to Figure 2 for location of raingauges and monitoring station. [Colour figure can be viewed at wileyonlinelibrary.com]

Table 4. Performance of debris flow rainfall triggering threshold (Gregoretti and Dalla Fontana, 2007) compared to available debris flow data (Table 3) and rainfall episodes recorded in the period 2014–2019 by raingauges 1, 2 and 3 (RG1, RG2 and RG3; see Figure 2 for location) as a function of the burst intensity threshold (BIT). tp = true positive; fn = false negative; fp = false positive; tn = true negative; fp + tn = number of rainfall burst episodes; AUC = area under the ROC curve; CSI$_{max}(\alpha)$ = maximum critical success index and corresponding value of the empirical constant α of the *ID* threshold equation ($I = \alpha D^{\beta}$).

BIT (mm per 5 min)	Triggering rainfalls tp/tp+fn	Non-triggering rainfalls RG1 fp/fp+tn	AUC	CSI$_{max}(\alpha)$	Non-triggering rainfalls RG2 fp/fp+tn	AUC	CSI$_{max}(\alpha)$	Non-triggering rainfalls RG3 fp/fp+tn	AUC	CSI$_{max}(\alpha)$
0.2	11/13	5/7278	0.995	0.67(22)	12/6300	0.984	0.59(22.4)	12/6286	0.959	0.55(21)
0.4	12/13	9/1883	0.995	0.48(22)	14/1888	0.985	0.46(21.4)	16/1826	0.937	0.50(23.6)
0.8	12/13	9/564	0.996	0.45(22)	14/569	0.982	0.43(21.4)	15/610	0.944	0.52(22)

surements 5 min after raingauge 1. On 4 August, the delay is more evident with a lag time of approximately 20 min. The maximum 5 min rainfall intensities measured for the two events are 106 mm h^{-1} (raingauge 2) and 110 mm h^{-1} (raingauge 1), respectively. It is also worth noting that raingauge 4 measured no rainfall on 23 July despite its short distance (3.4 km) from raingauge 1. Conversely, the rainfall that occurred on 4 August impacted a wider area, including the entire Mount Antelao massif, as demonstrated by two more debris-flow occurrences at San Vito di Cadore (Ru Secco creek; Gregoretti et al., 2018) and Vodo di Cadore (Rio Rudan creek). Other debris flows were also registered in the Ansiei valley, about 20 km northeast of Cancia.

On 23 July, the lag time between rainfall onset and debris flow occurrence (Figure 5), as recorded by the camera in the initiation area, was 20 min. Images (Figure 6) show the arrival of fast-flowing debris along the channel at the monitoring station. The pressure sensor PS02 buried in the channel bed measured the increase of basal pore fluid pressure up to 23.6 kPa, 25 s after the arrival of the first debris flow front. The pressure then decreased, until the sensor was swept away by the third surge that travelled down the channel just 38 s after the flow front. PS02 started measuring positive values of fluid pressure about 10 s before the arrival of the debris flow front (Figure 7). This trend indicates that no surface or saturated subsurface water flow was present prior to the arrival of the first surge.

Our images do not allow a precise measurement of velocity and flow depth. However, in the case of the propagation of easily distinguishable features such as debris flow fronts containing coarse particles, some velocity estimates were made based on frame-by-frame particle tracking and knowledge of the geometry of the framed area (Figure 7). Flow height was similarly estimated based on the geometry of the channel bed and banks. Data are referred to the pre-event channel topography and uncertainties are mainly associated with the actual shape of the cross-section contributing to the flow during the event.
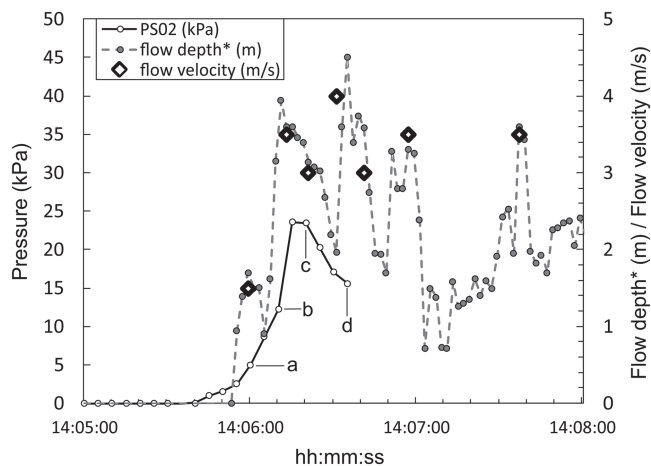

Figure 7. Fluid pressures measured by sensor PS02 buried in the channel bed during the transit of the debris flow front at the monitoring station on 23 July. Data are acquired every 5 s, the increase of fluid pressure is very rapid and reaches the peak after 35 s, shortly before the rupture of the cable occurred during the third surge. A short pressure decrease preludes the rupture of the cable that occurs during the passage of a second surge. Flow depth and velocity are estimated on the basis of image analysis of time-lapse videos. Letters in the figure refer to the images of Figure 6.

Assuming, as a first approximation, a horizontal cross-section profile, we found that the maximum errors for the flow velocities and flow depths reported in Figure 7 are about 0.4 m s^{-1} and 0.6 m, respectively. The comparison between basal pore fluid pressure and flow depth indicates that pressure was maintained well below the theoretical hydrostatic values. During the passage of the first surge, pressure steadily increased and peaked at 23.6 kPa during the transit of a second higher surge, for flow depths around 3–3.5 m. Subsequently, pore fluid pressure followed a trend similar to flow depth before the sensor was torn by the third surge.
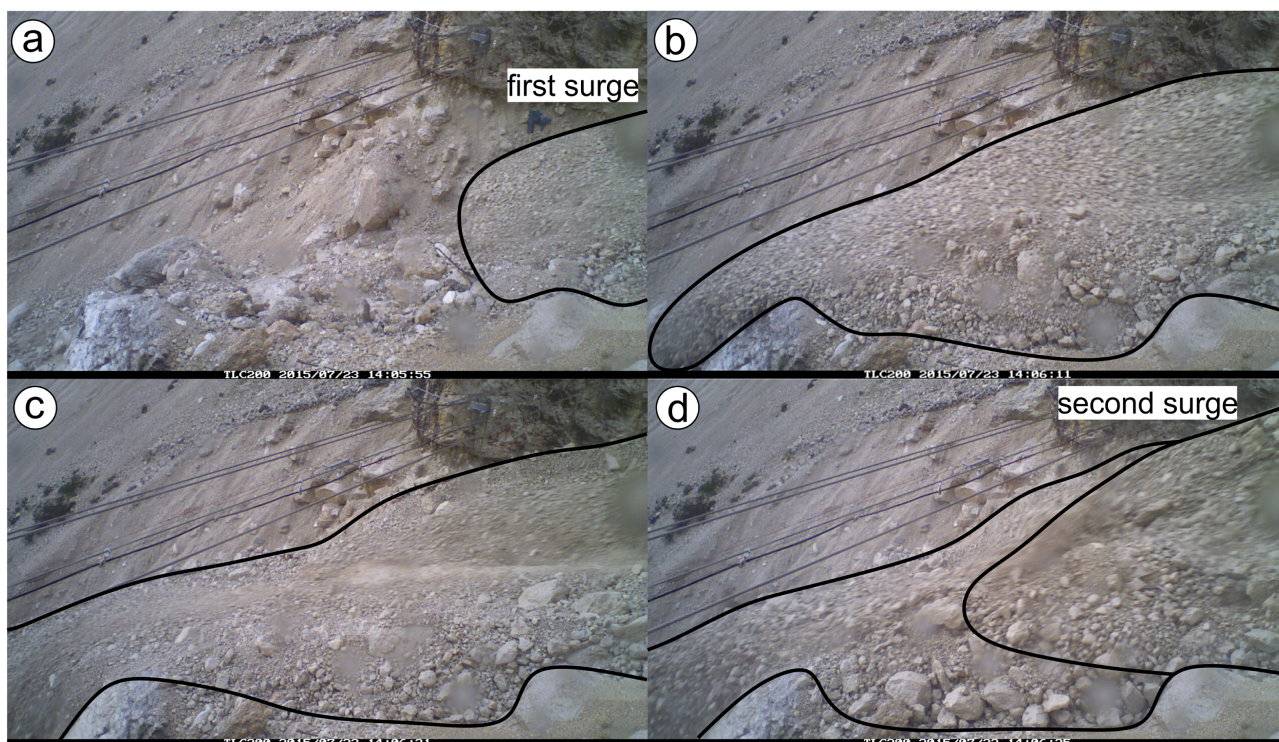

Figure 6. Images captured by the time-lapse camera at the monitoring station on 23 July. Black lines outline the flowing debris, frame letters are used in Figure 7 for comparison with fluid pressure measurements. [Colour figure can be viewed at wileyonlinelibrary.com]

The initial debris flow front propagated at $1.8\,ms^{-1}$, while the second surge travelled at $3–3.5\,ms^{-1}$, similar to the surges that followed. After the first three surges, the time-lapse video shows that sediment concentration dropped significantly, while the flow became gradually more irregular, resembling a hyperconcentrated streamflow (Pierson and Costa, 1987) with an occasional hint of surging behaviour. Flow discharge was sustained for 20–25 min before reducing to normal streamflow.

On 4 August, a time lag of 27 min separates the rainfall onset from the arrival of the sediment–fluid mixture in the initiation area. This longer time lag, as compared to the July event, is associated with a more gradual increase of rainfall intensity (Figure 5). Also, in this case, camera recordings show the sudden arrival of the flow front rather than the gradual increase of the runoff discharge. Basal pore fluid pressure data are not available because the pressure sensor was not yet replaced. The time-lapse images collected by the camera suggest quite immature flow conditions. The sediment–fluid flow was highly fluctuating, suggesting hyperconcentrated flow conditions (i.e. turbulent sediment-laden water flow). Coarse particle segregation is less recognizable at the front of incoming surges and estimated flow depth never exceeded 2 m. The flow lasted about 25 min and progressively diminishing runoff was observed afterwards. The 4 August event occurred at dusk and the fast flow is blurred in our images, due to increased exposure times. We are not including images as figures, but the reader can watch time-lapse videos of both events in the online Supporting Information.

In order to gain better insight into the different behaviour of the two debris flow events described so far, we used the event-based distributed hydrological model delineated in the methodological section to simulate the runoff delivered by the west sub-basin of Cancia. The computed runoff hydrographs are shown in Figure 8, together with the rainfall depth measured by raingauges 1 and 2 (Figure 2). The hydrographs refer to the channel section where the monitoring station is located.

The timing of the computed peak discharge fits very well with the arrival of the flow recorded at the monitoring station. This type of response has also been documented by Rengers *et al.* (2016) in steep catchments after wildfires and by Capra *et al.* (2018) for lahars. Figure 8 shows that simulated hydrographs are similar in terms of peak discharge. The overall shape is also similar, but the longer duration of the 4 August event produced a higher total water runoff (about 23%). Time-lapse videos also document the longer duration (about 5 min) of the second event. This can be explained by the different rainfall distributions: on 23 July the long tail probably does not contribute to runoff and the corresponding small rainfall depths infiltrate entirely. Indeed, because of the high abstraction observed in headwater basins like Cancia (Gregoretti *et al.*, 2016), a few millimetres difference in the tail of excess rainfall can sensibly influence the runoff volume.

Erosional–depositional dynamics

Repeated topographic surveys of the debris flow channel allow analysis of the morphological changes produced by the two successive events that occurred during 2015. Pre- and post-event channel topographies, in particular, were described by 1 m DEMs (Table 1) whose subtraction allowed us to obtain elevation-change models (Figure 9). These models give information about erosion and deposition patterns resulting from an entire event: debris flow front, successive surges and falling limb of the flow hydrograph. The results may be locally conservative for erosion and deposition because localized stream
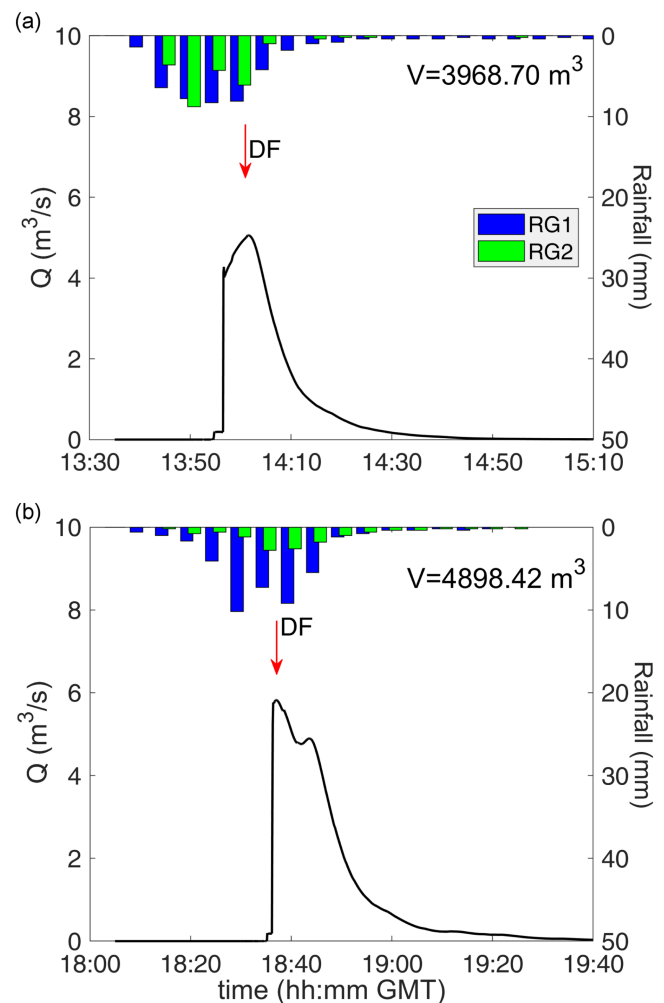

Figure 8. Runoff hydrographs simulated by means of the model of Gregoretti *et al.* (2016) for the two events of 23 July 2015 (a) and 4 August 2015 (b). In both cases, AMC conditions have been adopted as discussed in the text. The blue and green bars correspond to the rainfall depths sampled by raingauges 1 and 2, respectively. The timing of the observed debris/hyperconcentrated flow transits is pointed out by the red arrows. [Colour figure can be viewed at wileyonlinelibrary.com]

erosion or deposition may occur during the falling limb of the flow hydrograph (Berger *et al.*, 2011).

Overall, there is a reasonable agreement between total eroded and deposited volumes between the monitoring station and the lower retention basin, for the two events (Table 5). On 23 July, an excess 4400 m^3 of material was deposited while on 4 August, the deposition exceeded erosion of only 900 m^3. Differences between deposition and erosion volumes reflect the incoming volume of sediment at the monitoring station, with a higher volume likely characterizing the first event due to more mature flow conditions and higher sediment concentrations (Figure 6). However, since our observations do not include the portion of the headwater above the monitoring station (1675 m a.s.l.), we cannot exclude the influence of other possible triggering factors (e.g. rockfalls, dam break). At the same time, we recognize that excavation works carried out between the two events cause under-estimation of deposited material for the first event and over-estimation of eroded material for the second. Such inaccuracies are confined to the upper sediment retention basins and we estimate them in the order of 1000 m^3, less than 10% of the total deposited volume. The ranges of uncertainty reported in Table 5 derive from the accuracies of the DEMs used to calculate elevation-change models. They represent upper numerical limits since the actual
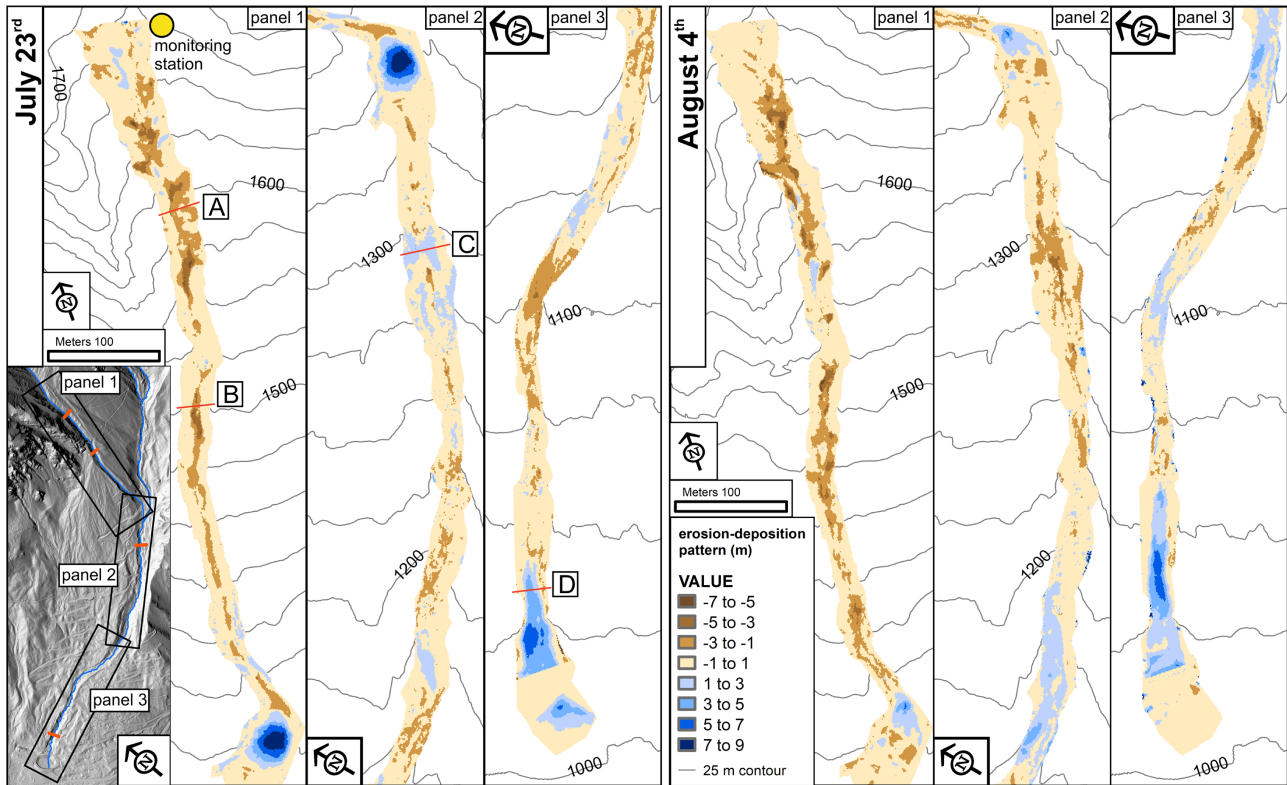
Figure 9. Channel elevation changes measured by subtraction of 1 m DEMs. The right inset shows the location of panels in the basin. The location of channel cross-sections of Figure 10 is reported in the panels of the 23 July event. [Colour figure can be viewed at wileyonlinelibrary.com]

Table 5. Results of DEM subtraction for the two debris flow events. The range of uncertainty has been evaluated following Wheaton *et al*. (2010)

	Area (m^2)			Volume (m^3)	
	Total	Erosion	Deposition	Erosion	Deposition
23 July	59952	29414	30538	22110 ± 9890	26506 ± 7950
4 August	59899	32470	27429	20909 ± 9545	21803 ± 8270

uncertainties are likely smaller owing to the typically random distribution of DEM inaccuracies.

Elevation-change maps (Figure 9) show that erosion is not evenly distributed along the channel. It clearly dominates from the initiation area to the upper retention basin (1340 m a.s.l.) where the average channel slope is 26.4(±3.6)°. The first event deposited about 6000 m^3 of material in the upper retention basin, while the second deposited only 2000 m^3 because the basin was largely filled up. Further downslope (1350–1050 m a.s.l.), the gully incision is less pronounced compared to the surrounding topography and the slope progressively decreases from about 20 to 12° (mean value = 15.9 ± 4.6°). Elevation-change models of the two events show scattered patches of alternating erosion and deposition. Overall, we observe substantial equilibrium along this reach. For both events, erosion-change models map a large deposit in the gentle final reach of the channel preceding the lower retention basin.

The comparison of overlapping sections in the channel (Figure 10) helps to illustrate the local significance of erosional–depositional dynamics. In the upper reach (section A), erosion deepens the channel bed, with maximum depth values of about 7 m for both events. Side erosion and induced failures along the gully flanks also contribute significant supply sediment to the debris flow. The erosive character of the flow is consistent along the channel down to the

upper retention basin, and occasional outcropping bedrock acts as a threshold for erosion. Further downstream, sediment accumulation and depletion occur alternately for the two successive events (section C). Whenever deposition becomes dominant, the channel rapidly fills up with sediment (section D), producing potential flow avulsion.

In order to analyse how erosion–deposition dynamics evolved along the channel, we integrated the information contained in our elevation-change models over successive 20 m-long sections of the debris flow channel. Results are expressed as net volume change (m^3) for each section or as specific volume change (SVC, m^3 m^{-1}). The latter is comparable with channel yield rate, originally introduced by Hungr *et al*. (1984) and later used by other authors (Bovis and Jakob, 1999; Marchi and D'Agostino, 2004; Breien *et al*., 2008) to describe the volume increase that a debris flow commonly experiences along its downslope path. By using the specific volume change, we also include information about the deposition rate – that is a measure of how much material was left behind by the debris flow along the channel whenever the slope gradient or the confinement diminish.

The specific volume change (Figure 11a) describes the clear erosive nature of the flow in the upper part of the channel. This was observed for both events with the highest values (about 50 m^3 m^{-1}) occurring where the channel gradient exceeds 25°. Scouring was almost regularly distributed along the upper
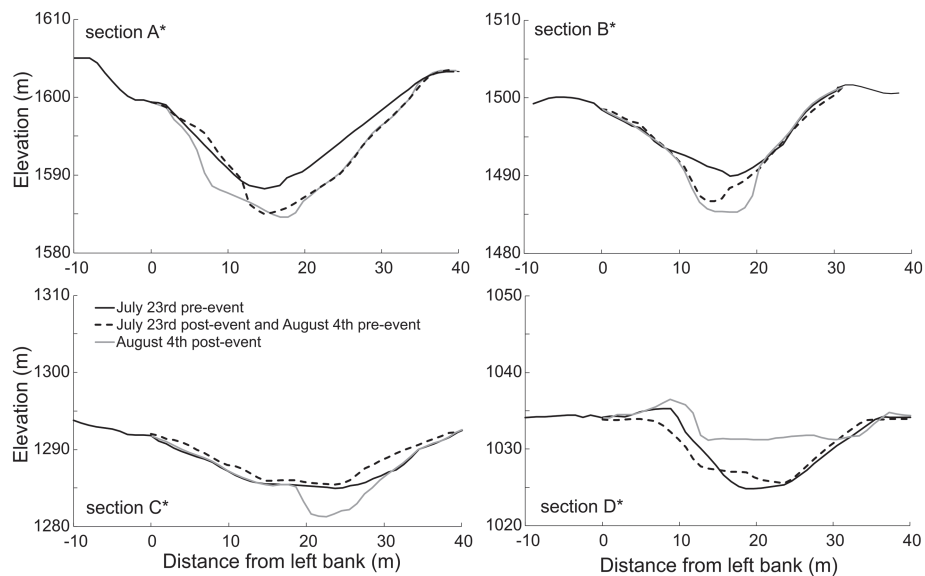
Figure 10. Examples of debris flow channel cross-sections comparing the pre- and post-event morphology. *Section location reported in Figure 9.
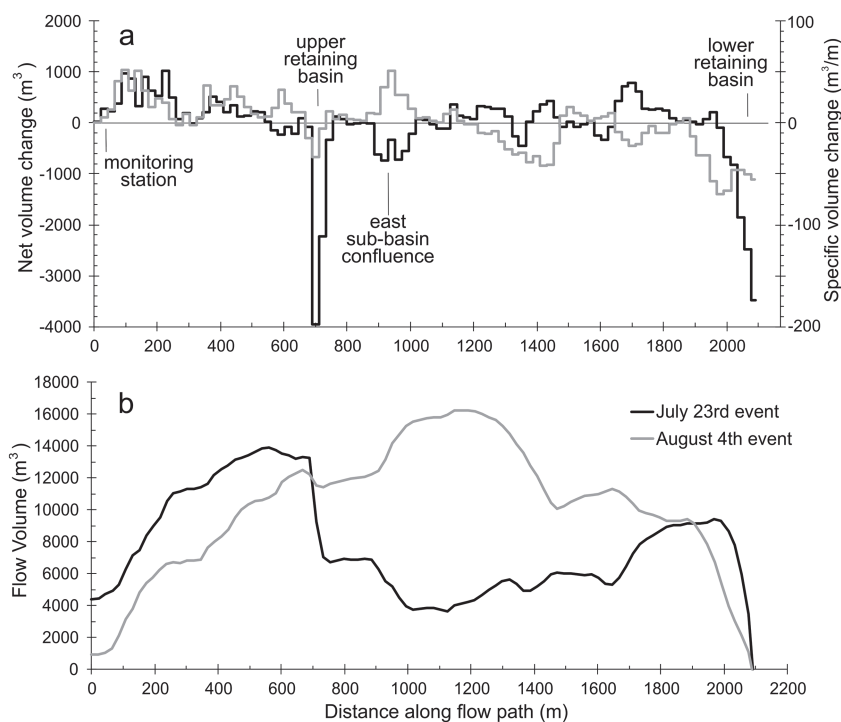
Figure 11. Volumetric relationship for the debris flow events of July 2015. (a) Net volume change calculated by DEM subtraction considering 20 m-long reaches. (b) Cumulative flow volumes obtained by summation of net volume changes; absolute values were determined by imposing null volume balance in the final deposition area (i.e. lower sediment retention basin). Apparent inconsistencies in the flow volume at the beginning of the surveyed channel reach (0 distance) are due to the mobilization of debris further upslope and/or volumetric error.

channel reach for both events, before sudden deposition took place at the upper sediment retention basin (Figure 11b). Further downstream, erosion and deposition alternated cyclically along reaches of length 150–250 m, with maximum values of about 40 m³ m⁻¹ for both erosion and deposition. In this portion of the debris flow channel, most of the sediment deposited by the July event was entrained by the August event. In turn, most of the sediment deposited by the August event was deposited where erosion by the previous event was more severe. About 8000 m³ of sediment was deposited by both events in the terminal reach of the channel and in the lower sediment retention basin.

The net change in volume that occurred from the initiation area, where our observations begin, allowed the calculation

of the cumulative volume of sediment transfer caused by the debris flow along its path (cumulative flow volume, in the following). Given that we have no measurement for the amount of water and sediment entering the initiation area, we imposed an equilibrium between erosion and deposition in the final deposition area and backward-added net volume changes. Inspection of the observed cumulative flow volumes (Figure 11b) of the two events reveals the non-perfect equilibrium between total entrained volume along the path and total volume deposited. The comparison of the cumulative flow volume for the two events shows that they reach similar values (13 300 and 12 500 m³, respectively) before deposition begins at the upper retention basin. Here the cumulative flow volume of the first event halved, whereas the second event deposited

only 1100 m^3 because the capacity of the retention basin was compromised. Further downstream, as already mentioned, erosion and deposition alternated for the two events. Their cumulative volume was similar (about 9000 m^3) before the final deposition took place.

Overall, the available data provide a complex erosion–deposition pattern for the two debris flows caused by multiple influencing factors. The channel slope has probably the most impacting role, as visualized in Figure 12 where bin-averaged (2.5° bin size) erosion/deposition rates are plotted against channel slope of the 20 m sections considered for the analysis. Flat areas corresponding to the sediment retention basins, together with a bedrock-incised channel reach, were excluded from the analysis. The plots describe the positive relationship between channel slope and specific volume change. Remarkably, the specific volume change exhibits a clear dependence from the slope angle of the channel bed (Figures 12c and d), with a positive, seemingly linear increase at slopes higher than 15–17°. At lower slopes, both erosion and deposition may occur, determining a closer equilibrium in terms of average specific volume changes.

Discussion

The Cancia debris flow basin has a long history of debris flow activity. We combined available historical information with 6 years of rainfall data to examine the separation between triggering and non-triggering rainfall events. Given the extreme rainfall intensities required for debris flow mobilization, the definition of rainfall parameters influences the relative positioning of a given rainfall event with respect to an intensity–duration triggering threshold. In general, it is preferable not to consider the whole rainfall event but only its most intense segment (or burst) by setting a minimum rainfall intensity value to identify the beginning and end of the burst (Coe *et al.*, 2008). In fact, light rain preceding or following the burst can significantly reduce the average rainfall intensity, modifying its position in comparison to a given triggering threshold. Based on our data, the use of a low burst intensity threshold, close to the accuracy of a raingauge (about 0.2 mm per 5 min), is beneficial to triggering rainfall identification, whereas the adoption of higher values tends to increase the number of false alarms, hindering the predictive performance of the triggering *ID* threshold. Our analysis at Cancia indicates that, despite showing a good predictive performance, the *ID* triggering threshold cannot perfectly separate triggering and non-triggering rainfalls (Figure 4 and Table 4). Possible factors contributing to generate erroneous predictions (false negatives or false positives) include physical variables such as antecedent rainfalls (Guo *et al.*, 2013) and debris availability (Ma *et al.*, 2018; Pastorello *et al.*, 2018) not accounted for by an *ID* threshold. Also, the timing of debris flow occurrence might be better suitable for truncating rainfall duration (Bel *et al.*, 2017; Raymond *et al.*, 2020). Finally, single raingauge measurements do not take into account the strong spatial variability of intense convective rainfalls. Our data clearly show such variability: in the case of the two debris flow events that occurred in 2015 at Cancia, three out of four raingauges operating in a restricted area (about 10 km^2) failed to measure the precipitation that actually triggered the events. Only the instrument located in the headwater basin, at higher elevations, recorded rainfalls sufficient to exceed the triggering thresholds (Figure 5). Other techniques of rainfall measurement (e.g. radar) may be more suitable to overcome this problem (Marra *et al.*, 2016; Destro *et al.*, 2017). However, rainfall spatial variability strongly impacts our ability to predict the occurrence of debris flows based on rainfall triggering thresholds, especially in case of convective rainstorms.

The two debris flows that occurred in July and August 2015 at Cancia were initiated along the channel by incoming discharge produced by intense rainstorms (Figure 5). The time
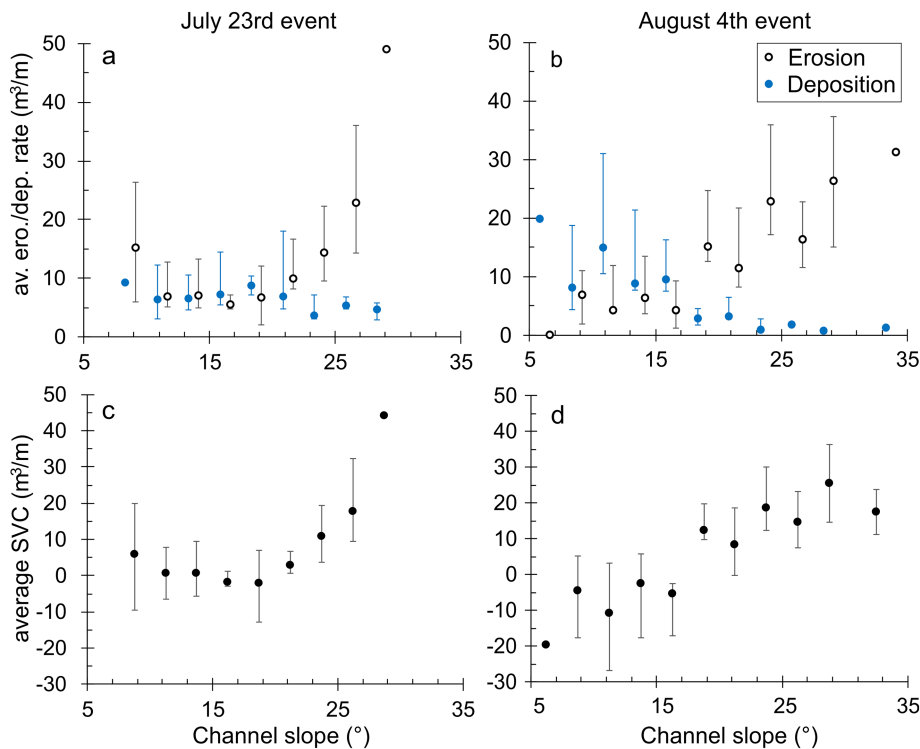

Figure 12. Relationship between channel slope and bin-averaged values of (a, b) erosion/deposition rates and (c, d) specific volume change (SVC) for the investigated debris flow events. Bins have a size of 2.5° and error bars represent the 25th and 75th percentiles. [Colour figure can be viewed at wileyonlinelibrary.com]

to peak discharge in the initiation area was similar for the two events and ranged between 20 and 27 min, as documented by monitoring data. The documentation of the first debris flow event includes the basal pore pressure record at the flow front (Figure 7). During the passage of the first surges, pressures maintained lower than hydrostatic, suggesting the importance of granular interactions in the initial stages of the flow in accordance with other available measures for natural debris flows (Berti *et al.*, 2000; McArdell *et al.*, 2007; McCoy *et al.*, 2013). This behaviour may be explained by the abundance of coarse particles that slide and collide with each other rather than being fully supported by fluid pressures.

The time-lapse videos recorded in the initiation area (see the online Supporting Information) clearly show the surging nature of the flows. In particular, videos show well-developed granular surges with abundant coarse particles during the July event while more immature surges, resembling a hyperconcentrated sediment-laden flow, were observed during the subsequent August event. During both events, flow characteristics differ among successive surges (Berger *et al.*, 2011; Imaizumi *et al.*, 2017) and a consistent trend of decreasing sediment concentration is observed until normal streamflow is eventually reached.

Downstream of the monitoring station, we have documented the erosion–deposition dynamics of the two events through elevation-change maps (Figure 9). Data can be used to analyse differences and similarities between the two events. On the one hand, different flow characteristics observed in the time-lapse videos are likely caused by the depletion of sediment along the channel bed upstream of the monitoring station, produced by the first event. Under reduced sediment availability conditions, a solid granular flow cannot fully develop and the sediment–fluid flow that develops is highly turbulent, fully saturated (Imaizumi *et al.*, 2019) and shows scarce to no coarse particle segregation. On the other hand, both events mobilized the majority of sediment along the upper channel between the monitoring station and the first sediment retention basin (about 700 m), where the slope exceeds 20°. Here, the erosion–deposition maps indicate that the two events showed a tendency to level their cumulative flow volume (Figure 11b). Given that the triggering runoff discharge was also not very dissimilar (Figure 8), the observations on the whole suggest that the supply of readily available sediment in the upper channel did not represent a severe limiting condition for the volume of the two debris flows, despite their close occurrence. Erosion and entrainment are confirmed as the dominant mechanisms contributing to debris flow bulking, as observed in other catchments (Hungr *et al.*, 1984). Given that they are widely distributed along the upper channel (Berger *et al.*, 2011; Iverson *et al.*, 2011), local lack or abundance of sediment can compensate, probably until the flow approaches an equilibrium concentration dependent on the channel slope (Takahashi, 1991).

In the upper reaches of the debris flow channel, the longitudinal bed slope appears as the major factor driving erosion. The relationship between channel slope and erosion rate (Figure 12) is sufficiently clear for slopes higher than 0.3 (about 16°) for both events. Also, Theule *et al.* (2015) analysed the relationship between erosion and slope but their results suggest that a proportionality holds at more moderate slope gradients (<0.21), whereas sediment supply limitation curbs erosion in steeper channels. The considerable scatter shown by the slope–erosion relationships indicates that other factors play a role and may give rise to complex interactions. They include flow discharge (Breien *et al.*, 2008; Schürch *et al.*, 2011), local channel morphology (He *et al.*, 2018; Ma *et al.*, 2018, Vázquez *et al.*, 2016), erodibility of the channel bed and pre-flow water content of bed sediment (McCoy *et al.*, 2012).

Along the transport reach of the debris flow channel, the slope is lower (<0.3) and the behaviour less clearly defined, with erosion and deposition prevailing alternately. Multiple factors surely contribute to determine this trend; they may include flow discharge (Breien *et al.*, 2008; Schürch *et al.*, 2011), local slope and channel geometry (Abanco and Hurlimann, 2014; Theule *et al.*, 2015; Vázquez *et al.*, 2016) and degree of saturation of the bed sediment (McCoy *et al.*, 2012). However, along the prevailing transport reach (about 1200 m), our data (Figures 9 and 11) indicate that sediment accumulation and erosion occur alternately for the two events. Where the first event deposited sediment, the second eroded and entrained the loose freshly deposited material. Where the first event entrained sediment, the second left behind debris deposits. This peculiar and antimetric behaviour indicates that sediment availability along the channel, at slope gradients lower than 0.3, strongly influenced the erosion–deposition dynamics at Cancia. Similar patterns were described by Imaizumi *et al.* (2019), who indicated repetitive mass movements and deposition episodes as responsible for debris flow surges along the channel.

The volumes of sediment mobilized by the two debris flows, as estimated through our elevation-change models (Figure 9), can be used together with the hydrological simulations (Figure 8) to quantitatively evaluate the average solid concentration (solid to liquid volumetric ratio) of the two events. With this aim, we considered the sediment eroded and entrained by the flow upstream of the east sub-basin confluence (i.e. where more water was delivered to the debris flow channel by the east sub-basin) and the water discharge concentrated in the west sub-basin, as simulated by the distributed model. Taking into account the uncertainties related to the porosity (0.3–0.4) and degree of saturation (0.5–0.7) of the entrained material, we obtained concentration values ranging between 0.54 and 0.64 for the first event and 0.49 and 0.59 for the second event. These estimates indicate that the average volume sediment concentrations are close for the two events and well in the range typically indicated for granular debris flows (McCoy *et al.*, 2013). In the spectrum included between supply-limited and transport-limited conditions (Bovis and Jakob, 1999), our data indicate that the two flows were closer to the second. However, the lower values of concentration obtained for the second event suggest that its volume was limited by the minor availability of sediment along the channel, due to the event that occurred just 12 days before.

Conclusions

By combining high-resolution measurements of topographic change of the debris flow channel with monitoring data from the initiation area, we document two events that occurred a few days apart in the summer of 2015 in the dolomitic catchment of Cancia.

Intensity–duration rainfall thresholds correctly identify the triggering precipitation events and demonstrate a good predictive performance, though triggering and non-triggering rainfall events are not perfectly separated due to the influence of other factors. Spatial rainfall variability is well documented by our data and may hinder the utility of rainfall thresholds depending on position and number of available raingauge measurements.

Cancia is a debris flow basin with abundant unconsolidated sediment. Elevation-change models show that the erosion and entrainment of sediment along the steep upper part of the channel represent the dominant mechanism determining debris flow progressive bulking. The erosion rate of the two events is influenced by the slope of the channel and such dependence is well

established at slopes higher than 16°. We did not find an upper slope limit to the growth of the erosion rate, which may be interpreted as evidence of transport-limited conditions. The integration and comparison of the observations of the two events describe a complex picture where liquid discharge and sediment availability interact along the channel to determine the debris flow volume. Local conditions of reduced sediment availability may initially produce turbulent low concentration sediment–fluid flows. However, the flows exhibited a tendency to approach an equilibrium concentration during propagation that compensates for local lack or abundance of sediment. Hydrological modelling and elevation change maps of the two events indicate that, along the erosive reach, the second event mobilized a smaller amount of sediment (−12%) despite the higher total liquid discharge (+26%), demonstrating a moderate but significant influence of sediment availability on debris flow volume.

Alternation between erosion and deposition characterizes debris flow propagation along the channel at lower slopes. Here, the two successive events exhibited an opposite erosion–deposition pattern that indicates how sediment availability can influence the dynamics of the flow also along the prevailing-transport reach.

Data Availability Statement

Data for this paper can be made available upon reasonable request.

Conflict of Interest

The authors declare no conflict of interest.

References

Abanco C, Hurlimann M. 2014. Estimate of the debris-flow entrainment using field and topographical data. *Natural Hazards* **71**: 363–383.

Bacchini M, Zannoni A. 2003. Relations between rainfall and triggering of debris-flow: case study of Cancia (Dolomites, Northeastern Italy). *Natural Hazards and Earth System Sciences* **3**: 71–79.

Bel C, Liébault F, Navratil O, Eckert N, Bellot H, Fontaine F, Laigle D. 2017. Rainfall control of debris-flow triggering in the Réal Torrent, Southern French Prealps. *Geomorphology* **291**: 17–32.

Berger CB, McArdell B, Schlunegger F. 2011. Direct measurement of channel erosion by debris flows, Illgraben, Switzerland. *Journal of Geophysical Research – Earth Surface* **116**: F01002.

Bernard M. 2018. Analysis and modelling of surface runoff triggering debris flows. PhD thesis, University of Padova. http://paduaresearch.cab.unipd.it/10682/

Berti M, Genevois R, LaHusen R, Simoni A, Tecca PR. 2000. Debris flow monitoring in the Acquabona watershed (Dolomites, Italian Alps). *Physics and Chemistry of the Earth, Part B: Hydrology, Oceans & Atmosphere* **25**: 707–715.

Berti M, Simoni A. 2005. Experimental evidences and numerical modelling of debris flow initiated by channel runoff. *Landslides* **2**: 171–182.

Blasone G, Cavalli M, Marchi L, Cazorzi F. 2014. Monitoring sediment source areas in a debris-flow catchment using terrestrial laser scanning. *Catena* **123**: 23–36.

Bovis MJ, Jakob M. 1999. The role of debris supply conditions in predicting debris flow activity. *Earth Surface Processes and Landforms* **24**: 1039–1054.

Brasington J, Langham J, Rumsby B. 2003. Methodological sensitivity of morphometric estimates of coarse fluvial sediment transport. *Geomorphology* **53**: 299–316.

Breien H, De Blasio V, Elerhoi A, Hoeg K. 2008. Erosion and morphology of a debris flow caused by a glacial lake outburst flood, Western Norway. *Landslides* **5**: 271–280.

Cannon SH, Kirkham RM, Parise M. 2001. Wildfire-related debris-flow initiation processes, Storm King Mountain, Colorado. *Geomorphology* **39**: 171–188.

Capra L, Coviello V, Borselli L, Márquez-Ramírez V-H, Arámbula-Mendoza R. 2018. Hydrological control of large hurricane-induced lahars: evidence from rainfall-runoff modeling, seismic and video monitoring. *Natural Hazards and Earth System Sciences* **18**: 781–794.

Chow VT, Maidment DR, Mays LW. 1988. *Applied Hydrology*. McGraw-Hill: New York.

Coe JA, Kinner DA, Godt JW. 2008. Initiation conditions for debris flows generated by runoff at Chalk Cliffs, central Colorado. *Geomorphology* **96**: 270–297.

Degetto M, Gregoretti C, Bernard M. 2015. Comparative analysis of the differences between using LiDAR and contour-based DEMs for hydrological modeling of runoff generating debris flows in the Dolomites. *Frontiers in Earth Sciences* **3**(21): 1–15.

Destro E, Marra F, Nikolopoulos EI, Zoccatelli D, Creutin JD, Borga M. 2017. Spatial estimation of debris flows-triggering rainfall and its dependence on rainfall return period. *Geomorphology* **278**: 269–279.

Gregoretti C, Dalla Fontana G. 2007. Rainfall threshold for the initiation of debris flows by channel-bed failure in the Dolomites. In *Debris-Flow Mitigation: Mechanics, Prediction and Assessment*, Chen CL, Major JJ (eds). Milpress: London; 11–21.

Gregoretti C, Degetto BM, Boreggio M. 2018. The debris flow occurred at Ru Secco Creek, Venetian Dolomites, on 4th August 2015: analysis of the phenomenon, its characteristics and reproduction by models. *Frontiers in Earth Science* **6**(80): 1–20.

Gregoretti C, Degetto M, Bernard M, Crucil G, Pimazzoni A, De Vido G, Berti M, Simoni A, Lanzoni S. 2016. Runoff of small rocky headwater catchments: field observations and hydrological modeling. *Water Resources Research* **52**: 8138–8158.

Gregoretti C, Stancanelli L, Bernard M, Degetto M, Boreggio M, Lanzoni S. 2019. Relevance of erosion processes when modelling in-channel gravel debris flows for efficient hazard assessment. *Journal of Hydrology* **568**: 575–591.

Guo XJ, Cui P, Li Y. 2013. Debris flow warning threshold based on antecedent rainfall: a case study in Jiangjia Ravine, Yunnan, China. *Journal of Mountain Science* **10**(2): 305–314.

He S, Wang D, Chang S, Fang Y, Lan H. 2018. Effects of the morphology of sediment-transporting channels on the erosion and deposition of debris flows. *Environmental Earth Sciences* **77**: 544.

Höhle J, Höhle M. 2009. Accuracy assessment of digital elevation models by means of robust statistical methods. *ISPRS Journal of Photogrammetry and Remote Sensing* **64**: 398–406.

Höhle J, Potuckova M. 2011. *Assessment of the Quality of Digital Terrain Models*. European Spatial Data Research, Amsterdam. Official Publication n° **60**: 1–91.

Hu W, Dong XJ, Xu Q, Wang GH, van Asch TWJ, Hicher PY. 2016. Initiation processes for run-off generated debris flows in the Wenchuan earthquake area of China. *Geomorphology* **253**: 468–477.

Hungr O, Morgan GC, Kellerhals R. 1984. Quantitative analysis of debris torrent hazards for design of remedial measures. *Canadian Geotechnical Journal* **21**: 663–677.

Hurlimann M, Abanco C, Moya J, Vilajosana I. 2013. Results and experiences gathered at the Rebaixader debris-flow monitoring site, Central Pyrenees, Spain. *Landslides* **11**: 939–953.

© 2020 John Wiley & Sons, Ltd.

Earth Surf. Process. Landforms, Vol. 45, 3556–3571 (2020)

Imaizumi F, Hayakawa YS, Hotta N, Tsunetaka H, Ohsaka O, Tsuchiya S. 2017. Interactions between the accumulation of sediment storage and debris flow characteristics in a debris-flow initiation zone, Ohya landslide body, Japan. *Natural Hazards and Earth System Sciences* **17**: 1923–1938.

Imaizumi F, Masui T, Yokota Y, Tsunetaka H, Hayakawa YS, Hotta N. 2019. Initiation and runout characteristics of debris flow surges in Ohya landslide scar, Japan. *Geomorphology* **339**: 58–69.

Imaizumi F, Sidle RC, Tsuchiya S, Ohsaka O. 2006. Hydrogeomorphic processes in a steep debris flow initiation zone. *Geophysical Research Letters* **33**: L10404.

Iverson RM, Reid ME, Logan M, LaHusen RG, Godt JW, Griswold JP. 2011. Positive feedback and momentum growth during debris-flow entrainment of wet bed sediment. *Nature Geoscience* **4**: 116–121.

Jakob M, Bovis M, Oden M. 2005. The significance of channel recharge rates for estimating debris-flow magnitude and frequency. *Earth Surface Processes and Landforms* **30**: 755–766.

Jakob M, Friele P. 2010. Frequency and magnitude of debris flows on Cheekye River, British Columbia. *Geomorphology* **114**: 382–395.

Jakob M, Weatherly H, Bale S, Perkins A, McDonald B. 2017. A multi-faceted debris-flood hazard assessment for Cougar Creek, Alberta, Canada. *Hydrology* **4**: 7.

Kean JW, McCoy SW, Tucker GE, Staley DM, Coe JA. 2013. Runoff-generated debris flows: observations and modeling of surge initiation, magnitude, and frequency. *Journal of Geophysical Research – Earth Surface* **118**: 2190–2207.

Kean JW, Staley DM, Cannon SH. 2011. In situ measurements of post-fire debris flows in southern California: comparisons of the timing and magnitude of 24 debris-flow events with rainfall and soil moisture conditions. *Journal of Geophysical Research – Earth Surface* **116**: F04019.

Lamb MP, Dietrich WE, Venditti JG. 2008. Is the critical Shields stress for incipient sediment motion dependent on channel-bed slope? *Journal of Geophysical Research – Earth Surface* **113**: F02008.

Lane SN, Westaway RM, Hicks DM. 2003. Estimation of erosion and deposition volumes in a large, gravel-bed, braided river using synoptic remote sensing. *Earth Surface Processes and Landforms* **28**: 249–271.

Lavigne F, Thouret JC. 2003. Sediment transportation and deposition by rain triggered lahars at Merapi Volcano, Central Java, Indonesia. *Geomorphology* **49**: 45–69.

Loye A, Jaboyedoff M, Theule JI, Liébault F. 2016. Headwater sediment dynamics in a debris flow catchment constrained by high-resolution topographic surveys. *Earth Surface Dynamics* **4**: 489–513.

Ma C, Deng J, Wang R. 2018. Analysis of the triggering conditions and erosion of a runoff-triggered debris flow in Miyun County, Beijing, China. *Landslides* **15**: 2475–2485.

Mantovani F, Pasuto A, Silvano S. 2002. Definition of the elements at risk and mitigation measures of the Cancia debris flow (Dolomites, Northeastern Italy). In *Engineering Geology for Developing Countries – 9th Congress of the International Association for Engineering Geology and the Environment, Durban, South Africa*, van Rooy JL, Jermy CA (eds); 1201–1209.

Mao L, Cavalli M, Comiti F, Marchi L, Lenzi MA, Arattano M. 2009. Sediment transfer processes in two Alpine catchments of contrasting morphological settings. *Journal of Hydrology* **364**: 88–98.

Marchi L, D'Agostino V. 2004. Estimation of debris flow magnitude in the Eastern Italian Alps. *Earth Surface Processes and Landforms* **29**: 207–220.

Marra F, Nikolopoulos EI, Creutin JD, Borga M. 2016. Space–time organization of debris flows-triggering rainfall and its effect on the identification of the rainfall threshold relationship. *Journal of Hydrology* **541**: 246–255.

McArdell BW, Bartelt P, Kowalski J. 2007. Field observations of basal forces and fluid pore pressure in a debris flow. *Geophysical Research Letters* **34**: L07406.

McCoy SW, Kean JW, Coe JA, Tucker GE, Staley DM, Wasklewicz TA. 2012. Sediment entrainment by debris flows: in situ measurements from the headwaters of a steep catchment. *Journal of Geophysical Research – Earth Surface* **117**: F03016.

McCoy SW, Tucker GE, Kean JW, Coe JA. 2013. Field measurement of basal forces generated by erosive debris flows. *Journal of Geophysical Research – Earth Surface* **118**: 589–602.

NRCS. 2008. *National Engineering Handbook Part 630: Hydrology*. U.S. Department of Agriculture: Washington, D.C.

Okano K, Suwa H, Kanno T. 2012. Characterization of debris flows by rainstorm condition at a torrent on the Mount Yakedake volcano, Japan. *Geomorphology* **136**: 88–94.

Orlandini S, Rosso R. 1996. Diffusion wave modeling of distributed catchment dynamics. *Journal of Hydrologic Engineering* **1**: 103–113.

Panizza M, Piacente S, Silvano S, Siorpaes C, Toffoletto F, Bozzo GP. 1998. La frana di Borca di Cadore (Belluno), 7 August 1996. *Memorie della Società Geolica Italiana* **53**: 465–478.

Pastorello R, Hurlimann M, D'Agostino V. 2018. Correlation between the rainfall, sediment recharge, and triggering of torrential flows in the Rebaixader catchment (Pyrenees, Spain). *Landslides* **15**: 1921–1934.

Pierson TC, Costa JE. 1987. A rheologic classification of subaerial sediment-water flows. In *Debris Flows/Avalanches: Process, Recognition, and Mitigation*, Costa JE, Wieczorek GF (eds), Vol. **7**, Reviews in Engineering Geolology. Geological Society of America: Boulder, CO; 1–12.

Raymond CA, McGuire LA, Youberg AM, Staley DM, Kean JW. 2020. Thresholds for post-wildfire debris flows: insights from the Pinal Fire, Arizona, USA. *Earth Surface Processes and Landforms* **45**(6): 1349–1360. https://doi.org/10.1002/esp.4805

Recking A. 2009. Theoretical development on the effect of changing flow hydraulics on incipient bed load motion. *Water Resources Research* **45**: W04401.

Rengers FK, Kean JW, Reitman NG, Smith JB, Coe JA, McGuire LA. 2020. The influence of frost weathering on debris flow sediment supply in an alpine basin. *Journal of Geophysical Research: Earth Surface* **125**: e2019JF005369.

Rengers FK, McGuire LA, Kean JW, Staley DM, Hobley DEJ. 2016. Model simulations of flood and debris flow timing in steep catchments after wildfire. *Water Resources Research* **52**: 6041–6061.

Rickenmann D. 2016. Debris-flow hazard assessment and methods applied in engineering practice. *International Journal of Erosion Control Engineering* **9**: 80–90.

Schürch P, Densmore AL, Rosser NJ, Lim M, McArdell BW. 2011. Detection of surface change in complex topography using terrestrial laser scanning: application to the Illgraben debris-flow channel. *Earth Surface Processes and Landforms* **36**: 1847–1859.

SCS. 1972. *National Engineering Handbook Section 4: Hydrology* (NEH-4). U.S. Department of Agriculture: Washington, D.C.

Staley DM, Kean JW, Cannon SH, Schmidt KM, Laber JL. 2013. Objective definition of rainfall intensity–duration thresholds for the initiation of post-fire debris flows in southern California. *Landslides* **10**: 547–562.

Staley DM, Wasklewicz TA, Coe JA, Kean JW, McCoy SW, Tucker GE. 2011. Observations of debris flows at Chalk Cliffs, Colorado, USA: part 2, changes in surface morphometry from terrestrial laser scanning in the summer of 2009. In *Debris-flow Hazards Mitigation, Mechanics, Prediction, and Assessment*, Genevois R, Hamilton DL, Prestininzi A (eds). IOS Press: Amsterdam; 759–768.

Swets JA. 1988. Measuring the accuracy of diagnostic systems. *Science* **240**(4857): 1285–1293.

Takahashi T. 1991. *Debris Flow*. IAHR Monograph Series. Balkema: Rotterdam.

Theule JI, Liebault F, Laigle D, Loye A, Jaboyedoff M. 2015. Channel scour and fill by debris flows and bedload transport. *Geomorphology* **243**: 92–105.

Tognacca C, Bezzola GR, Minor H-E. 2000. Threshold criterion for debris-flow initiation due to channel-bed failure. In *Proceedings of the 2nd International Conference on Debris-Flow Hazard Mitigation, Taipei, Taiwan, 16–18 August*. Balkema: Rotterdam; 89–97.

Tropeano D, Maraga F, Turconi L. 1999. Eventi di piena e frana osservati nel 1999 nell' Italia settentrionale. *GEAM-Geoingegneria Ambientale e Mineraria* **95**: 1–121.

Underwood SJ, Schultz MD, Berti M, Gregoretti C, Simoni A, Mote TL, Saylor AM. 2016. Atmospheric circulation patterns, cloud-to-ground lightning, and locally intense convective rainfall associated with debris flow initiation in the Dolomite Alps of northeastern Italy. *Natural Hazards and Earth System Sciences* **16**: 509–528.

Vázquez R, Capra L, Coviello V. 2016. Factors controlling erosion/deposition phenomena related to lahars at Volcán de Colima, Mexico. *Natural Hazards and Earth System Sciences* **16**: 1881–1895.

Wheaton JM, Brasington J, Darby SE, Sear DA. 2010. Accounting for uncertainty in DEMs from repeat topographic surveys: improved sediment budgets. *Earth Surface Processes and Landforms* **35**: 136–156.

Supporting Information

Additional supporting information may be found online in the Supporting Information section at the end of the article.

Data S1 Supporting Information